SUPPLEMENT TO THE *WELDING JOURNAL,* APRIL 2016
Sponsored by the American Welding Society and the Welding Research Council

WELDING RESEARCH

A Residual Stress Study in Similar and Dissimilar Welds

To gain more knowledge of residual stresses in dissimilar joints, welds between carbon steel and austenitic stainless steel were examined using the neutron diffraction method

BY H. EISAZADEH, J. BUNN, H. E. COULES, A. ACHUTHAN, J. GOLDAK, AND D. K. AIDUN

ABSTRACT

Residual strain distributions in similar and dissimilar welds were measured using the neutron diffraction (ND) method. Then, using three strain components, three-dimensional stress states were calculated. The results were used to determine the effect of the martensitic phase transformation and material properties on residual stress (RS) distribution. It was observed that smaller longitudinal RS was induced in the low-carbon steel side of the dissimilar weld when compared to its similar weld. Also, it was found that the transverse RS near and within the weld zone (WZ) in the dissimilar weld exhibited a distinctive trend, with tensile mode reaching the yield strength of the base metal (BM). In order to characterize the WZ in the dissimilar weld, optical microscopy, hardness tests, and energy dispersive x-ray spectroscopy (EDAX) were employed. This study not only provides further insight into the RS state in similar and dissimilar welds, it also delivers important consequences of phase transformation in the latter case.

KEYWORDS

• Neutron Diffraction • Dissimilar Weld • Residual Strain and Stress

Introduction

Fabrication of structural components using dissimilar steels delivers structures that are lighter and more economical. Dissimilar weld joints such as stainless steel to carbon steel are being used in the petrochemical and power generation industries (Refs. 1, 2).

Joining of dissimilar metals/alloys is generally more challenging than similar alloys (Refs. 3, 4), which is due to several factors, such as the differences in chemical compositions and physical properties. Furthermore, welding of dissimilar steels produces different residual stress (RS) distributions in welds as compared with welding of similar metals, and this merits investigation of RS distribution in dis-

similar welds.

Several studies on the effect of RS on the failure of dissimilar weld joints have been reported (Refs. 5–8). For instance, Suzuki et al. (Ref. 9) reported significant stress corrosion cracking as a result of RS in the dissimilar welds between ferritic steels and austenitic stainless steels, which are widely used in the oil and gas industry. Lately, a number of studies have used numerical models based on FEM analysis to predict RS in dissimilar welds. Deng et al. (Ref. 10) determined the RS in a dissimilar metal pipe joint considering cladding, buttering, and postweld heat treatment. Similarly, Lee et al. (Ref. 11) predicted the axial and hoop RS produced in a high-strength carbon steel pipe weld using a FE model by

employing a sequentially coupled 3D thermal and solid-state phase transformation during welding. Generally, numerical techniques to estimate RS have been developed to a degree of sophistication, which are shown in the aforementioned publications. However, material modeling has always been a critical issue in the simulation of welding because of the scarcity of material data at elevated temperatures. Some simplifications and approximations are usually introduced to cope with these problems. These simplifications are necessary due to both lack of data and numerical problems when trying to model the actual high-temperature behavior of the material. As a result, the effect of modeling idealizations can cause differences between modeling and experimental results. In addition, these discrepancies might increase when it comes to dissimilar welds because of uncertain material properties, uncertain chemical composition, and uncertain phase composition in the weld zone (WZ) and the heat-affected zone (HAZ). In numerical modeling of dissimilar welds, these are normally ignored due to lack of corresponding experimental data. For example, the European Network on Neutron Techniques Standardization for Structural Integrity (NET) showed the predicted stresses even in similar welds are sensitive to the numerical modeling assumptions and boundary conditions (Ref. 12).

There are some previous works evaluating RS in dissimilar welds using experimental methods such as x-ray diffrac-

H. EISAZADEH, A. ACHUTHAN, and D. K. AIDUN (daidun@clarkson.edu) are with Department of Mechanical and Aeronautical Engineering, Clarkson University, Potsdam, N.Y. J. BUNN is with Chemical and Engineering Materials Division, Oak Ridge National Laboratory, Oak Ridge, Tenn. H. E. COULES is with Solid Mechanics Research Group, University of Bristol, Bristol, UK. J. GOLDAK is with Carleton University, Ottawa, Ontario, Canada.
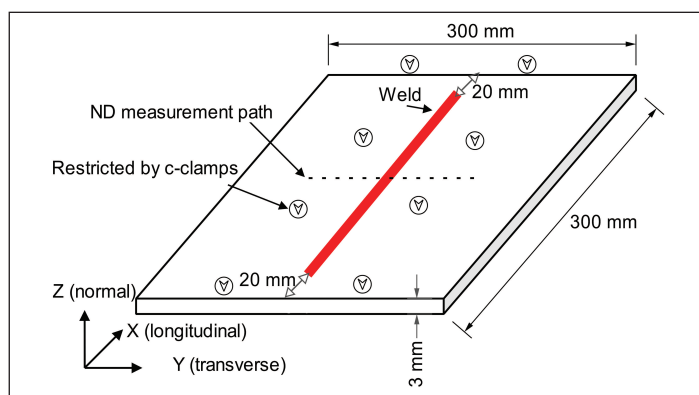
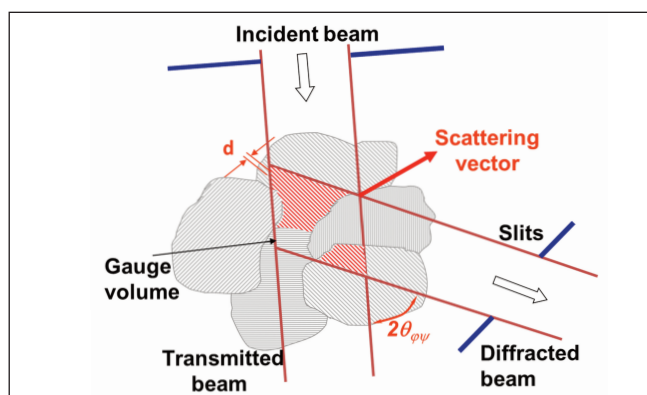Fig. 1 — Dimensions and measurement directions of the specimen.

Fig. 2 — Scattering vector for a Bragg reflection. From a single crystallographic plane family, from Ref. 26 with permission from Anna Paradowska.

tion, hole-drilling, and ultrasonic measurement (Refs. 13, 14). However, neutron diffraction (ND) is outstanding among these techniques because of its ability to obtain RS nondestructively within the interior of components, in three dimensions, in small test volumes, and in thick specimens (up to several cm) (Ref. 15). In this study, in order to gain further insight into the RS of dissimilar welds, three welds (similar and dissimilar welds of low-carbon steel and austenitic stainless steel) were created, and characterized using optical microscopy, hardness testing, energy-dispersive x-ray spectroscopy (EDAX) and ND. This work is concentrated on RS distribution in dissimilar welds. It also explores how the material properties, phase transformation due to weld dilution in dissimilar welds can contribute in RS formation. Moreover, RS states in the corresponding similar welds were examined for comparison purposes.

Experimental

Material and Welding Procedures

Experimental work was carried out on three butt joint welds, using low-carbon (AISI 1018) and austenitic stainless steel (AISI 304) plates. The experiment layout and material compositions of the alloys are shown in Tables 1 and 2, respectively. Single-pass autogenous gas tungsten arc (GTA) welding was used for all cases. The welding parameters (Table 3) were designed so as to produce partial penetration since no auxiliary argon gas was accommodated for weld protection underneath. After welding, the specimens were allowed to cool for 2000 s, after which time the temperature had approximately equilibrated, before being released from the C-clamps. Dimensions of samples are shown in Fig. 1.

Microstructure of Similar and Dissimilar Welds

It is important to analyze the microstructure of the welds prior to ND measurement in view of the fact that this measurement focuses on specific lattice plane spacings of a subset of grains, with specific orientations relative to the scattering vector — Fig. 2. This ability to actively select specific hkl lattice planes allows the separation of the strain responses of different phases in a multiphase material — Fig. 2. In some cases, each phase in a multi-phase material, such as duplex steel, which roughly consists of a 50/50 mixture of austenite phase and δ-ferrite phase, can carry different stresses (Ref. 15). In this study, since the material consists of single phase, except the WZ of the dissimilar weld, only a single lattice plane is required to be used for the ND measurement.

Optical microscopy, microhardness measurements, EDAX analysis, and the Schaeffer diagram were used to

Table 1 — Experiment Layout

Cases	Material
Case-1	Similar weld of 1018 steel
Case-2	Similar weld of 304 stainless steel
Case-3	Dissimilar weld of 304 stainless steel and 1018 steel

Table 2 — Chemical Composition of Steel Plates (wt-%)

Composition	C	Mn	Si	P	S	Cr	Ni	Balance	Ni_{eq}	Cr_{eq}
1018 steel (average)	0.13–0.20	0.30–0.90	0.15–0.30	0–0.04	0–0.05	—	—	Fe	≈6	0.3
304 stainless (average)	0–0.08	1.7	0.52	0–0.045	0–0.035	18.9	7.5	Fe	≈10	≈20
1018-304 WZ (EDAX)	—	1.14	0.12	—	—	7.58	4.32	Fe	≈7	≈8
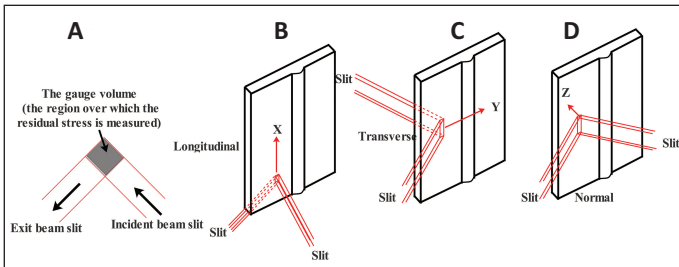
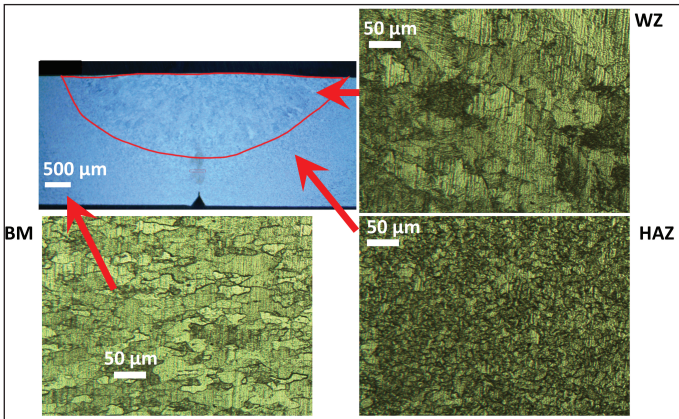Fig. 3 — A — Gauge volume definition and B–D — scattering vectors used in this study.
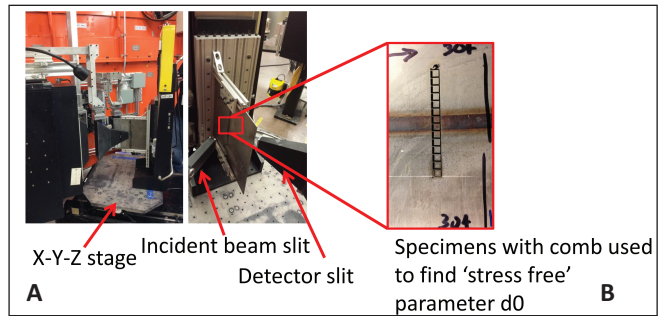

Fig. 4 — Experimental setup for neutron-diffraction measurements at Oak Ridge National Laboratory.

Fig. 5 — Macrostructure and microstructure of 1018 similar weld, etchant 2% Nital.
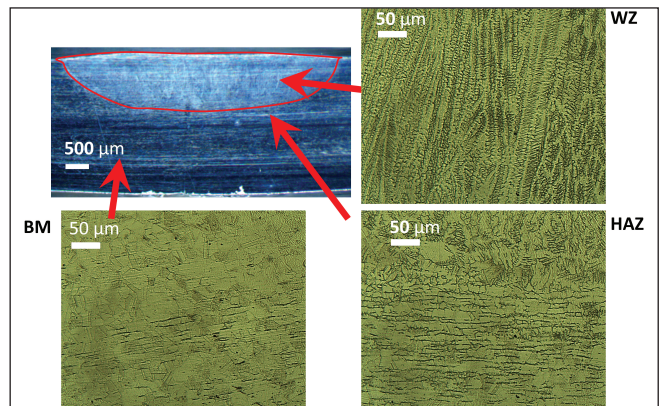

Fig. 6 — Macrostructure and microstructure of 304 similar weld, etchant 87% Glyceregia.

identify the phases, compositions present in the weldment in similar welds and dissimilar welds. Since mostly ferrite and austenite were present in 1018 similar welds and 304 similar welds, respectively, a single lattice plane was used for each similar weld. The (211) and (311) planes are suitable for ferritic and austenitic plates since these two planes approximate the elastic strain response of the bulk material, and are not sensitive to intergranular strains (Ref. 15). In the ferritic-austenitic dissimilar weld, a new phase (martensite) was present in the WZ; the ND setup was not changed to capture this small region. Therefore, the measurement was run again with (211) plane in 1018 side and (311) plane in 304 side.

Neutron Diffraction Measurement

Neutron diffraction (ND) has benefits such as deep penetration (centimeters) into many engineering materials, three-dimensional mapping, and volume-averaged bulk measurement capabilities. These characteristics make ND a powerful tool for the measurements of RS at depth in welds (Ref. 15). In this study, the ND measurements were carried out at the high flux isotope reactor (HFIR) of Oak Ridge National Laboratory on the second generation neutron residual stress facility (NRSF2). The beam geometry and the samples mounted in the fixture are shown in Figs. 3 and 4, respectively. The sample translation stage and goniometer are able to perform precision

motions (0.01 mm) for the placement of an instrumental gauge volume. The gauge volume is defined by a set of Gd slits. In the experiment, two different gauge volume geometries were utilized — Fig. 3. The gauge volume geometry was chosen dependent on the strain direction being measured. For the transverse and normal directions, a gauge volume of $1 \times 1 \times 4$ mm (width, depth, and height) was used. The extended height is along the direction of the weld and is the direction of symmetry in the sample. For the longitudinal case, the gauge volume was changed to $1 \times 1 \times 1$ mm so the height would be coincidental with the welding direction.

The incident wavelength for the instrument is defined by a bent silicon crystal focusing monochromator (Ref.

Table 3 — Welding Parameters Used in This Study

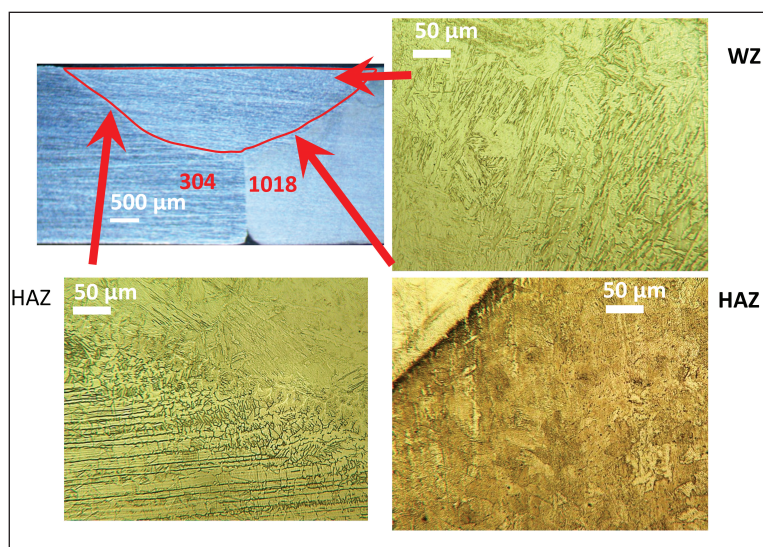| Arc Voltage (V)	Arc Current (A)	Electrode Diameter (mm)	Arc Length (mm)	Travel Speed (mm/s)	Argon Gas (m³/s)	Arc Efficiency
18	150	2.4	1.5	4	0.0136	80% (Ref. 19)

Fig. 7 — Macrostructure and microstructure of 304-1018 dissimilar weld, etchant 2% Nital and 87% Glyceregia.
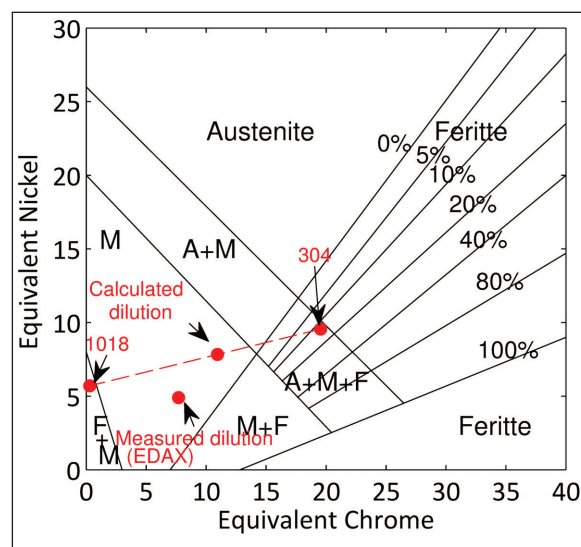

Fig. 8 — Estimation of weld zone phases using the Schaeffler diagram.

Table 4 — Diffraction Elastic Constants Used in This Study (Ref. 15)

Material	(hk)l	E^{hk}_l	v^{hk}_l
1018 steel	Fe (211)	225.5 GPa	0.28
304 stainless steel	Fe (311)	183.5 GPa	0.31

16). For the experiment, a wavelength of 1.73 Å was used. This defines the Fe (211) reflection at a 2θ of ~95.1° for the 1018 side and the Fe (311) reflection at a 2θ of ~106° for the 304 side. At each measurement point, lattice strains were calculated from the corresponding d-spacing changes in three orthogonal directions (Fig. 3) such that the stress fields could be calculated. The lattice strain can be determined from the measured lattice spacing according to (Ref. 15):

$$\varepsilon_{ii} = \frac{d - d_o}{d_o} = -\cot\theta \ (\theta - \theta_o) \quad i = 1,2,3$$

(1)

where the d and d_o are the interplanar spacing under the stressed and stress-free state, respectively. And θ and θ_o are the diffraction angles for the stressed and stress-free specimens at each location, respectively (Ref. 15). Since d_o is required as a reference in ND strain calculation, it was determined using a macroscopic "stress-free" comb-like coupon, as shown in Fig. 4. Each comb-like coupon was cut from a nominally

identical weld at the same locations as the ND measurements using electric discharge machining (EDM). The coupon has been sliced 3 mm wide and 3 mm thick along the transverse direction in order to release the macroscopic stresses effectively from the bulk of the weldment. With the assumption that the three orthogonal components of measured strain correspond to principal directions, meaning the shear stresses are assumed zero in these defined directions, the analysis to determine RS is simplified. The macroscopic stress components, where the numerical superscripts refer to the lattice plane family, are related to the elastic strains in analogy with Hooke's Law by Ref. 15:

$$\sigma_{ij} = \frac{E^{hkl}}{(1 + v^{hkl})}$$

$$\left[\varepsilon_{ij} + \delta_{ij} \frac{v^{hkl}}{(1 - 2v^{hkl})} \varepsilon_{kk} \right]$$

(2)

where E^{hkl} and v^{hkl} are the diffraction elastic constants' relating strain in the

(311) and (211) lattice planes to the macroscopic stress. And also ε_{ij} and ε_{kk} in the above equations are the elastic bulk strains. These elastic constants may be either measured or calculated with a good accuracy based on the self-consistent Kröner model and using single crystal elastic constants for austenitic stainless steel and low carbon steel (Ref. 15). The values used in this study are shown in Table 4

Results

Macro and Microstructure Studies of the Welded Samples

Macrostructure and microstructure of the three cases (Table 1), are shown in Figs. 5–7. For these three joints, it can be seen that the WZs are different from one another. For instance, the depth of penetration in similar 1018, similar 304, and 1018-304 dissimilar, are 1.7, 0.9, and 1.53 mm, respectively. Different depths and weld shapes are attributed to the different thermal physical properties of the base metals (BMs). In the dissimilar weld, the WZ and HAZ are asymmetric, and the deepest penetration is located off the weld centerline with larger WZ in the 304 side, as the thermal conductivity of the 304 is much less than 1018. This phenomenon is studied in detail by Bahrami et al. (Ref. 17).

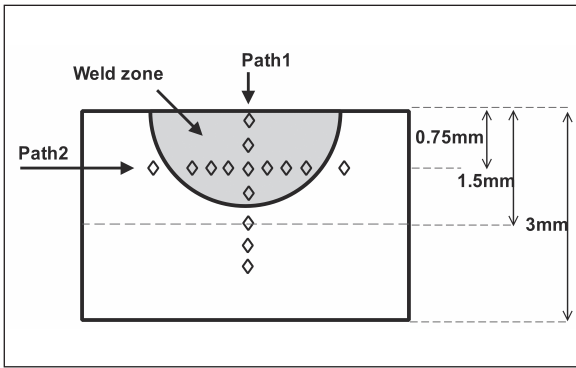The BM of 1018 weldment has microstructures of ferrite and pearlite, as

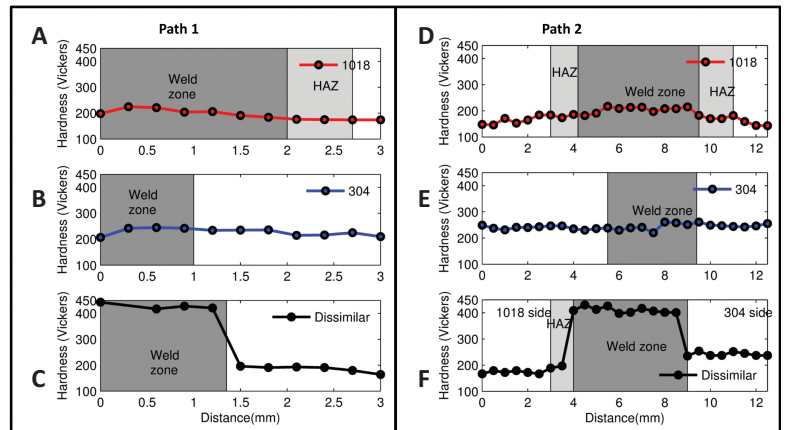Fig. 9 — Microhardness measurement (paths 1, 2).

Fig. 10 — Microhardness profiles of 1018 similar, 304 similar, and 1018-304 dissimilar welds cross section. Profiles A, B, and C were taken along path 1, shown in Fig 9. Profiles D, E, and F were taken along path 2, shown inFig. 9. Error of all microhardness measurements is ±20HV.

shown in Fig. 5. The WZ contains coarse pearlite as a result of an intermediate cooling rate to room temperature, while the HAZ contains fine pearlites due to a faster cooling rate. Since ferrite was mostly present in the BM, HAZ, and WZ of 1018 similar weld, the (211) Bragg reflection was used for ND measurement.

Figure 6 shows the microstructure of the 304 weldment. It is well known that the microstructure of 304 is mainly composed of single-phase austenite. However, this austenitic microstructure contains a small amount of δ-ferrite. Figure 6 also shows a columnar dendritic structure within the WZ. This is attributed to the fact that, during weld metal solidification, some supercooling effects occur. Since the austenite phase was available in all three regions (BM, HAZ, and WZ), the ND measurements used the (311) Bragg reflection.

Figure 7 shows the macro and microstructure of the 304-1018 dissimilar welds. The Schaeffler diagram was used to predict the microstructure of the WZ for dissimilar welds. To calculate dilution, cross-sectional areas of the melted 304 BM and 1018 BM were calculated with the aid of *ImageJ* (image analysis software) (Ref. 18). Calculation showed approximately 43% dilution from 1018 and 56% dilution from 304 BM. Considering the composition of the BM, Cr_{eq} and Ni_{eq} were evaluated. Three points, representing the microstruc-

tures for the 1018, 304, and dilution of dissimilar weld, are shown in Fig. 8. According to EDAX analysis, the result of which is shown in Table 2, Cr_{eq} and Ni_{eq} were calculated. These results are plotted in Fig. 8, which are in good agreement with the measured dilution. According to the Schaeffler diagram, dissimilar WZ is martensitic. Strain and stress carried by this phase was not captured with ND measurement since only ferrite and austenite phases were considered.

Microhardness Test

Hardness profiles can assist the interpretation of weld microstructures and mechanical properties. In this work, several metallographic specimens were prepared from each weldment. Microhardness tests were performed by measuring values across the weld cross section, crossing both the HAZ and WZ for the three cases — Table 1. The Vickers test was measured with a load of 500 gf and a loading time of 10 s along both paths 1 and 2, as shown in Fig. 9. Microhardness profiles across the three weldments are shown in Fig. 10. From the profiles of Fig. 10A (path 1) and Fig. 10D (path 2), it was observed the hard-

ness of similar 1018 weldment slightly increases from BM to WZ. This is due to increasing the density of pearlite within the WZ. Hardness in the 304 similar weld, shown in Fig. 10B (path 1) and Fig. 10E (path 2), has essentially no variation throughout the weldment. However, in the case of the 304-1018 dissimilar weld, a sharp increase (about 200 HV) can be seen crossing the HAZ and WZ of the weldment — Fig. 10C, F. The reason behind this increase could be due to formation of martensite in the WZ, which confirms the microstructure determined by the Schaeffler diagram.

Neutron Diffraction

Interplanar Spacing and Stress-Free Spacing

Figures 11–13 show the variation of the interplanar spacing (d) in three directions for similar and dissimilar welds measured by ND along mid-thickness of plates. Note that the interface between all three welds was marked as 0 mm. The results of the macroscopic stress-free spacing (d_o), which was measured from the reference coupon

Table 5 — Mechanical and Thermal Properties of 1018 and 304 at Room Temperature (Ref. 21)

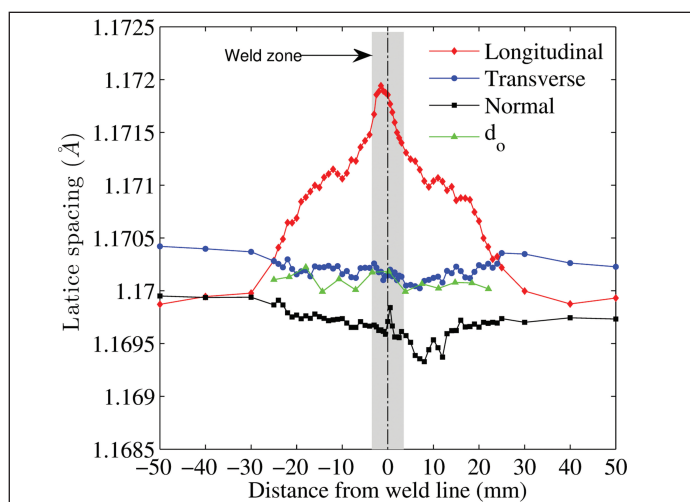| Material	Thermal Conductivity, W/m. °K	Thermal Expansion Coefficient, 1×10^{-6}/°K	Yield Strength, MPa
1018 steel	52	10	250
304 stainless	17	20	320

Fig. 11 — Distribution of the interplanar spacing (d and d$_o$) in 1018 similar weld. Error of lattice spacing measurement is ± 1 × 10^{-4}Å.
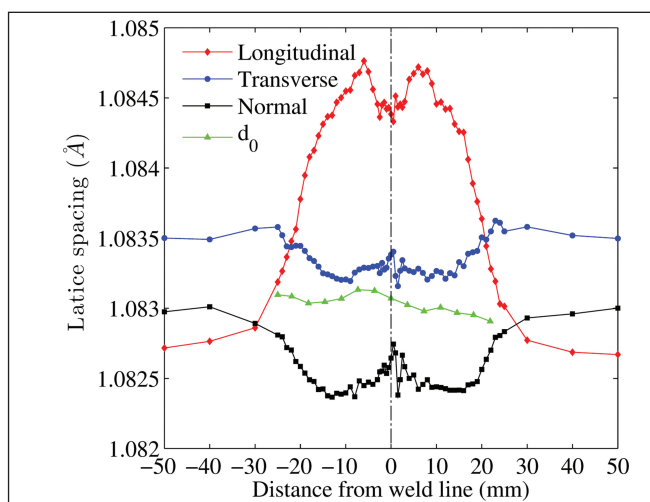

Fig. 12 — Distribution of the interplanar spacing (d and d$_o$) in 304 similar weld. Error of lattice spacing measurement is ± 1 × 10^{-4}Å.
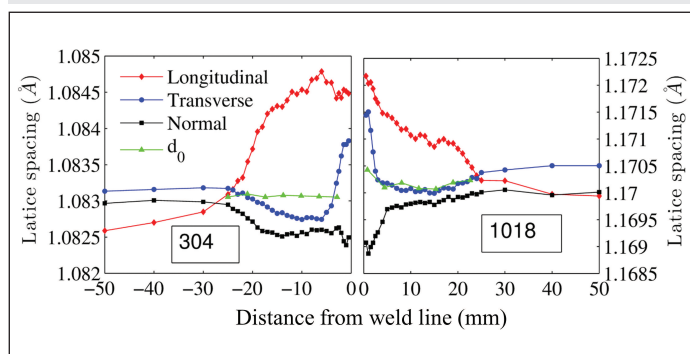

Fig. 13 — Distribution of the interplanar spacing (d and d$_o$) in 304-1018 dissimilar weld. Distance zero is the WZ. Error of lattice spacing measurement is ± 1 × 10^{-4}Å. The lattice place measured in 304 and 1018 sides are (311) and (211), respectively.
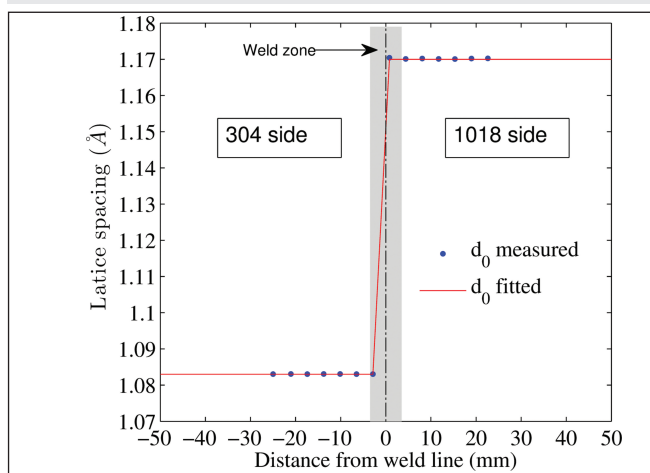

Fig. 14 — Distribution of the interplanar spacing (d$_o$) and its fitted curve in 304-1018 dissimilar weld. The fitted curved was considered for strain calculations in dissimilar weld. Distance zero is the WZ. Error of lattice spacing measurement is ± 1 × 10^{-4}Å.

specimens, are shown within ±25 mm away from the weld centerline. The reason is the chemical composition of BM outside of this zone (±25 mm) is far from the process affected zone, and d_0 does not change considerably. Therefore, the measured d_0 at location 25 mm can be extended for the rest of the BM for strain and stress calculations. In Figs. 11–13, the d of the longitudinal component is clearly higher than the other two components (transverse and normal).

The asymmetry observed in the 304 similar weld d_0 measurement is most likely due to some heterogeneous gauge volume effects. This is expected in the 304 case due to heterogeneous changes in the phase fraction of δ-ferrite in the weld region. Typically, if one extent of the gauge volume has a reduced amount of grains contributing to diffraction, it will lead to an artificial shift of the gauge volume. In this case, the shift is due to an increase in δ-ferrite.

The d_0 values for the dissimilar weld are difficult to obtain and index vs. the measured d-spacings. This is because the unstressed spacings are measured from an analog plate, where the 304-1018 transition is difficult to position, and may not occur in the same position as in the dissimilar measurement sample. To overcome this challenge, a stress balance approach was used to define the actual center of the d_0 sample. The measured d_0 values and the interpreted values are shown in Fig. 14.

Strain

Using Equation 1, three stain components (longitudinal, transverse, and normal) of the similar and dissimilar weldments are calculated and plotted in Figs. 15–17, respectively. First, three strain components of two similar welds are addressed. Then, the results of the dissimilar weld are presented.

As anticipated, the longitudinal residual strain of all three cases is in tensile mode near the WZ (±25 mm). The longitudinal strain width of the 304 weld is wider than the 1018 weld. This is mainly due to higher CTE of 304 than that of 1018. The transverse residual strains of both 1018 similar and 304 similar welds are in tensile mode, as well. However, their magnitudes are smaller than the longitudinal component. The reason is the contraction due to material shrinkage in the longitudi-
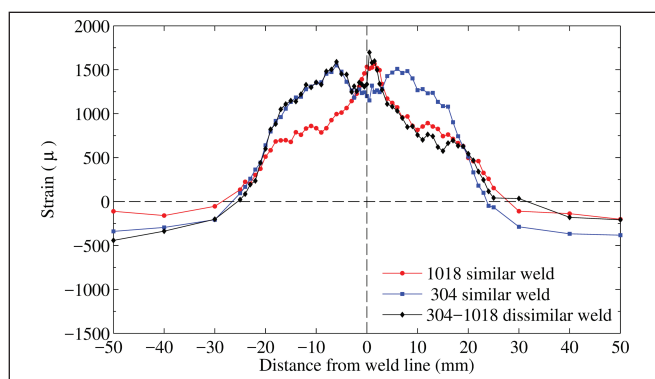
Fig. 15 — Distribution of longitudinal strain in 1018 similar, 304 similar, and 304-1018 dissimilar weld. Error of strain measurement is ± 100μ.
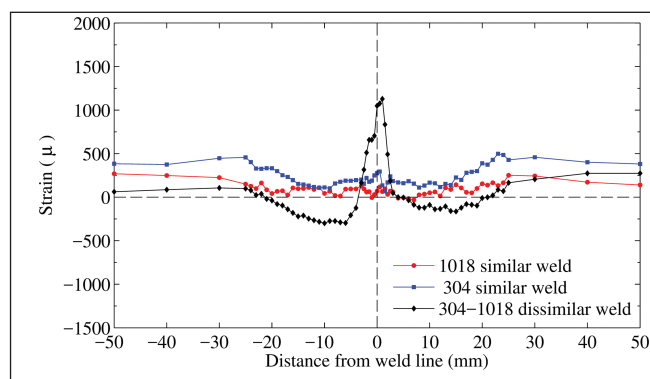

Fig. 16 — Distribution of transverse strain in 1018 similar, 304 similar, and 304-1018 dissimilar weld. Error of strain measurement is ± 100μ

nal direction is greater than that of the transverse direction. The normal strain components of all three cases are in compressive mode (±30 mm) due to the Poisson effect.

It is interesting to note the longitudinal residual strain in the 1018 side of the dissimilar weld (Fig. 15) experienced a residual strain reduction (between 10 and 20 mm away from the weld centerline). This fact was discussed by Eisazadeh et al. (Ref. 19). Another interesting point is the transverse residual strain in the dissimilar weld underwent a sharp increase near the WZ (±30 mm). These two points will be discussed in more detail below.

Stress

Using Equation 2, three stress components (longitudinal, transverse, and normal) of similar and dissimilar welds are calculated and plotted in Figs. 18–20, respectively.

The individual stress components do not follow the same trends seen in the corresponding strain components, due to the contribution of three strain components in Equation 2. The aforementioned fact about stress reduction in the dissimilar weld is clearly shown in Fig. 18.

Discussion

Similar Weld

The similar weld of 1018 steel shows the maximum value of residual longitudinal stress is limited to a small region (±7 mm) near the weld centerline (Fig. 18). However, in the 304 similar weld, this zone is extended to a wider area (±20 mm). The reason behind this fact

is that 304 stainless steel has a larger CTE and yield strength, yet lower thermal conductivity than the 1018 steel. Since the CTE has a significant effect on the RS, and this property of 304 is much greater when compared to the 1018 (Table 5), the RS in the 304 weld is increased remarkably to a high value. Lower thermal conductivity of 304 could boost the RS in the 304 sample since it leads to higher thermal gradients. Also, heat capacity is lower for 304 leading to higher temperatures for a given energy input. These cause the area near the weld interface of the 304 sample to remain at high temperatures, whereas away from the weld interface it remains cool (Ref. 20). Therefore, the region near the weld interface experiences a high temperature gradient, which causes higher RS.

Dissimilar Weld

Generally, when a dissimilar weld is carried out, residual stresses induced by the arc welding process could produce different RS distributions, especially near the WZ. This is due to the different CTE and yield strength of the base metals, as described clearly in the previous study (Ref. 20). Figure 18 shows a large stress reduction on the 1018 side of the dissimilar weld. This is because during the weld thermal cycle, the 304 plate, which has a larger CTE, can produce a tensile load on the 1018 side of the weld, while placing itself into a state of compression. It has been shown that the application of tensioning load during the welding process can greatly reduce the longitudinal tensile RS in friction stir welded joints (Refs. 19, 21, 22).

Beside these two material properties, the microstructure of the WZ in a dissimilar weld can contribute significantly to RS formation near the weld interface (Ref. 23). In Fig. 7, it was shown the microstructure of the WZ in the dissimilar weld sample is mainly martensitic because of the varied composition and rapid cooling. This hypothesis was confirmed with the microhardness test, shown in Fig. 10C and F. When the face-centered cubic structure of the WZ (austenite) transforms to the body-centered tetragonal structure (martensite) during cooling, a volume expansion is experienced. This increase produces a compressive stress within the WZ, however, it induces a tensile stress to the surrounding area.

It was shown the martensite was not present throughout the plate because of partial penetration of the WZ, as shown in Fig. 7. So, during ND measurement, the RS within the ferritic and austenitic phases of the surrounding area were captured because the gauge volume overlaps the BM and the WZ. Although gauge volume includes the WZ (martensite) partially, the compressive stress within the WZ was not recorded because it was neither the ferritic nor austenitic phases, and the ND measurement indicates only stresses within the selected phase within the gauge volume. This is shown in Fig. 2. A single phase measurement was all that was carried out in this experiment. A complete representation of multiple phases' contribution to residual stress could be determined using a time-of-flight neutron diffractometer, such as the VULCAN diffractometer at the Spallation Neutron Source, and performing a Rietveld re-
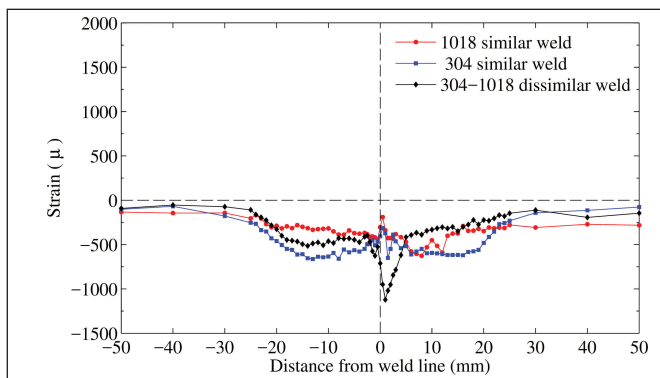
Fig. 17 — Distribution of normal strain in 1018 similar, 304 similar, and 304-1018 dissimilar weld. Error of strain measurement is ± 100μ.

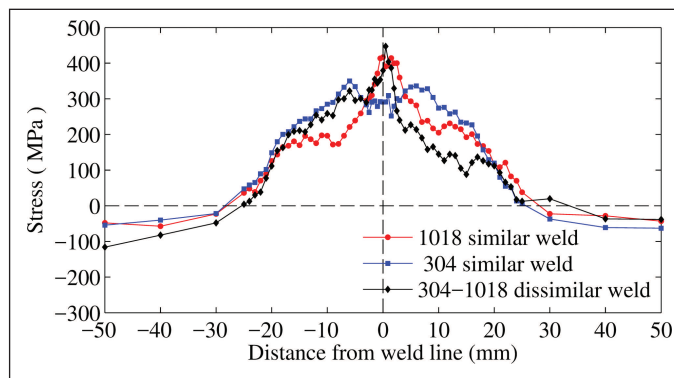
Fig. 18 — Distribution of longitudinal stress in 1018 similar, 304 similar, and 304-1018 dissimilar weld. Error of stress measurement is ± MPa.
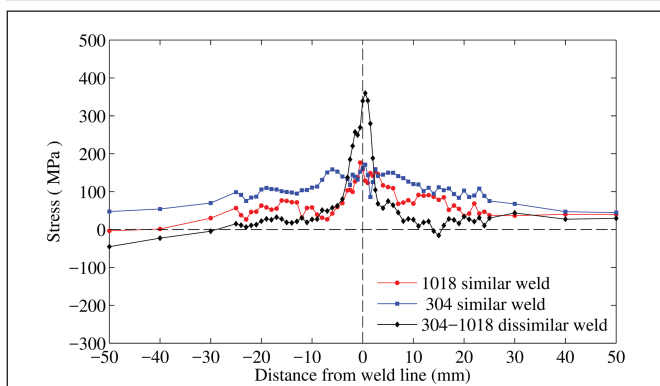

Fig. 19 — Distribution of transverse stress in 1018 similar, 304 similar, and 304-1018 dissimilar weld. Error of stress measurement is ± MPa.
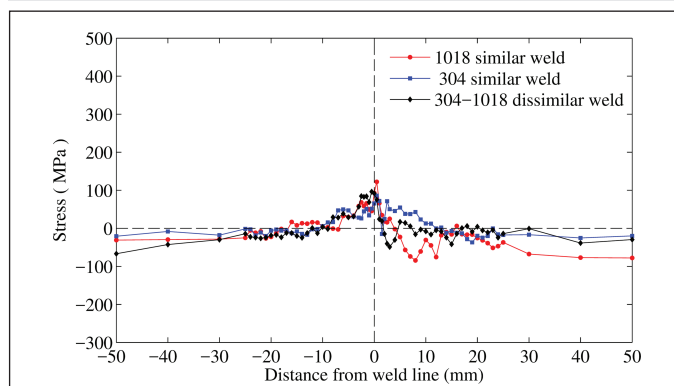

Fig. 20 — Distribution of normal stress in 1018 similar, 304 similar, and 304-1018 dissimilar weld.

finement to determine the lattice parameter shift, taking into account multiple phases (Refs. 24, 25). However, this method was not used in this study because the required neutron gauge volumes are currently unachievable at VULCAN.

Conclusions

In this study, residual strain and stress distributions of similar and dissimilar welds were measured using neutron diffraction. Effects of phase transformation and material properties on residual stress distributions in the dissimilar welds were addressed. The following conclusions were reached:

1) The tensile region of residual stresses in the longitudinal direction extends much further from the weld center in the case of the similar 304 weld than in the similar 1018 weld, due to the differences in thermal and mechanical properties between the two materials, such as CTE, thermal conductivity, and heat capacity.

2) Asymmetric residual stress distributions were observed in the dissimilar weld, which was caused by differences in CTE, yield strengths, and thermal conductivity of the two base metals.

3) The transverse residual stresses induced by welding exhibited distinctive trends between the similar and dissimilar welds, which is attributed to existence of martensite phase in the latter.

4) In the dissimilar weld, the CTE plays a role on stress reduction in the 1018 side by introducing a tensioning load caused by the 304 plate.

References

1. Zhang, T., Brust, F. W., Wilkowski, G., Huang, C.-C., Liu, R.-F., Ranganath, S., Wang, L., and Tsai, Y. L. 2012. Weld residual stress analysis and the effects of structural overlay on various nuclear power plant nozzles. *Journal of Pressure Vessel Technology* 134(6); 061205. doi:10.1115/1.4006558.

2. Khalifeh, A. R., Dehghan, A., and Hajjari, E. 2013. Dissimilar joining of AISI 304L/St37 steels by TIG welding process. *Acta Metallurgica Sinica* (English Letters) 26(6): 721–727.

3. Woo, W., Em, V., Hubbard, C. R., Lee, H.-J., and Park, K. S. 2011. Residual stress determination in a dissimilar weld overlay pipe by neutron diffraction. *Materials Science and Engineering* A 528(27): 8021–8027.

4. Sedek, P., Brozda, J., Wang, L., and Withers, P. J. 2003. Residual stress relief in

MAG welded joints of dissimilar steels. *International Journal of Pressure Vessels and Piping* 80(10): 705–713.

5. Jang, C., Lee, J., Kim, J. S., and Jin, T. E. 2008. Mechanical property variation within Inconel 82/182 dissimilar metal weld between low alloy steel and 316 stainless steel. *International Journal of Pressure Vessels and Piping* 85(9): 635–646.

6. Jang, C., Cho, P.-Y., Kim, M., Oh, S.-J., and Yang, J.-S. 2010. Effects of microstructure and residual stress on fatigue crack growth of stainless steel narrow gap welds. *Materials & Design* 31: 1862–1870.

7. Saji, G. 2009. Degradation of aged plants by corrosion: "Long cell action" in unresolved corrosion issues. *Nuclear Engineering and Design* 239(9): 1591–1613.

8. Warke, R. W., Hart, J. D., and Thacker, B. H. 2006. Probabilistic Assessment of a 70-year-old pipeline subject to seismic deformation. *Integrity Management*. Poster Session; Student Paper Competition. ASME, Vol. 2. pp. 743–754.

9. Suzuki, H., Katsuyama, J., and Morii, Y. 2012. Comparison of residual stress distributions of similar and dissimilar thick butt-weld plates. *Journal of Solid Mechanics and Materials Engineering* 6(6): 574–583.

10. Deng, D., Ogawa, K., Kiyoshima, S., Yanagida, N., and Saito, K. 2009. Prediction of residual stresses in a dissimilar metal welded pipe with considering cladding, buttering and post weld heat treatment. *Computational Materials Science* 47(2): 398–408.

11. Lee, C.-H., and Chang, K.-H. 2011. Prediction of residual stresses in high strength carbon steel pipe weld considering solid-state phase transformation effects. *Computers & Structures* 89(1): 256–265.

12. Smith, M. C., Smith, A. C., Wim-pory, R., and Ohms, C. 2014. A review of the NeT Task Group 1 residual stress measurement and analysis round robin on a single weld bead-on-plate specimen. *International Journal of Pressure Vessels and Piping* 120-121(8–9): 93–140.

13. Ranjbarnodeh, E., Serajzadeh, S., Kokabi, A. H., Hanke, S., and Fischer, A. 2011. Finite element modeling of the effect of heat input on residual stresses in dissimilar joints. *The International Journal of Advanced Manufacturing Technology* 55(5): 649–656.

14. Javadi, Y., Najafabadi, M. A., and Akhlaghi, M. 2012. Residual stress evaluation in dissimilar welded joints using finite element simulation and the LCR ultrasonic wave. *Russian Journal of Nondestructive Testing* 48(9): 541–552.

15. Hutchings, M. T., Withers, P. J., Holden, T. M., and Lorentzen, T. 2005. *Introduction to the Characterization of Residual Stress by Neutron Diffraction.* CRC Press.

16. Popovici, M., Stoica, A. D., Hubbard, C. R., Spooner, S., Prask, H. J., Gnaeupel-Herold, T. H., Gehring, P. M., and Erwin, R. W. 2001. Multiwafer focusing neutron monochromators and applications. *International Symposium on Optical Science and Technology*. International Society for Optics and Photonics. pp. 21–32.

17. Bahrami, A., and Aidun, D. K. 2014. Modeling of carbon steel duplex stainless steel GTA weld pool. *Welding Journal* 94(7): 262-s to 270-s.

18. Rasband, W. S. 2012. WS 1997-2012. *ImageJ*, U.S. National Institutes of Health, Bethesda, Maryland.

19. Eisazadeh, H., Achuthan, A., Goldak, J. A., and Aidun, D. K. 2015. Effect of material properties and mechanical tensioning load on residual stress formation in GTA 304-A36 dissimilar weld. *Journal of Materials Processing Technology* 222(8): 344–355.

20. McDill, J. M. J., Oddy, A. S., Goldak, J. A., and Bennison, S. 1990. Finite element analysis of weld distortion in carbon and stainless steels. *The Journal of Strain Analysis for Engineering Design* 25(1): 51–53.

21. Price, D. A., Williams, S.W., Wescott, A., et al. 2007. Distortion control in welding by mechanical tensioning. *Science and Technology of Welding & Joining* 12(7): 620–633.

22. Altenkirch, J., Steuwer, A., Peel, M., Richards, D. G., and Withers, P. J. 2008. The effect of tensioning and sectioning on residual stresses in aluminium AA7749 friction stir welds. *Materials Science and Engineering* A 488(1–2): 16–24.

23. Venkata Ramana, P., Madhusudhan Reddy, G., Mohandas, T., and Gupta, A. V. S. S. K. S. 2010. Microstructure and residual stress distribution of similar and dissimilar electron beam welds — Maraging steel to medium alloy medium carbon steel. *Materials and Design* 31(2): 749–760.

24. Daymond, M. R., Bourke, M. A. M., Von Dreele, R. B., Clausen, B., and Lorentzen, T. 1997. Use of Rietveld refinement for elastic macrostrain determination and for evaluation of plastic strain history from diffraction spectra. *Journal of Applied Physics* 82(4): 1554.

25. Rietveld, H. M. 1969. A profile refinement method for nuclear and magnetic structures. *Journal of Applied Crystallography* 2(2): 65–71.

26. Price, J. W. H., Ziara-Paradowska, A., Joshi, S., Finlayson, T., Semetay, C., and Nied, H. 2008. Comparison of experimental and theoretical residual stresses in welds: The issue of gauge volume. *International Journal of Mechanical Sciences* 50(3): 513–521.